Publ. Astron. Soc. Japan (2021) 73 (2), 405–416
doi: 10.1093/pasj/psab007
Advance Access Publication Date: 2021 February 16

A high-speed and high-efficiency imaging polarimeter based on ferroelectric liquid crystal retarders: Design and test

Jing Guo,[1,2] Deqing Ren,[3,*] Yongtian Zhu,[1,2,4] and Xi Zhang[1,2]

[1]National Astronomical Observatories/Nanjing Institute of Astronomical Optics & Technology, Chinese Academy of Sciences, Nanjing 210042, China
[2]CAS Key Laboratory of Astronomical Optics & Technology, Nanjing Institute of Astronomical Optics & Technology, Nanjing 210042, China
[3]Physics & Astronomy Department, California State University Northridge, Northridge, CA 91330, USA
[4]University of Chinese Academy of Sciences, Beijing 100049, China

*E-mail: ren.deqing@csun.edu

Received 2020 February 20; Accepted 2021 January 8

Abstract

Polarimeters play a key role in investigating solar magnetic fields. In this paper, a High speed and high efficiency Imaging POlarimeter (HIPO) is proposed based on a pair of ferroelectric liquid crystal retarders (FLCs), with the ultimate goal of measuring magnetic fields of prominences and filaments from the ground. A unique feature of the HIPO is that it enables high cadence polarization measurements covering a wide field of view (FOV); the modulation frequency of the HIPO is able to achieve ∼100 Hz, which greatly suppresses the seeing-induced crosstalk, and the maximum FOV can reach $62'' \times 525''$. Additionally, FLC retardances under low and high states were calibrated individually and found to have a slight discrepancy, which is neglected in most works. Based on FLC calibration results, an optimization was performed using a constrained nonlinear minimization approach to obtain the maximum polarimetric efficiency. Specifically, optimized efficiencies of the Stokes *Q*, *U*, and *V* are well balanced and determined as $(\xi_Q, \xi_U, \xi_V) = (0.5957, 0.5534, 0.5777)$, yielding a total efficiency of 0.9974. Their practical efficiencies are measured as $(\xi_{Q'}, \xi_{U'}, \xi_{V'}) = (0.5934, 0.5385, 0.5747)$, slightly below the optimized values but still resulting in a high total efficiency of 0.9861. The HIPO shows advantages in terms of modulation frequency and polarimetric efficiency compared with most other representative ground-based solar polarimeters. In the observations, measurement accuracy is found to be better than 2.7×10^{-3} by evaluating full Stokes Hα polarimetry results of the chromosphere. This work lays a foundation for the development of high-speed and high-accuracy polarimeters for our next-generation solar instruments.

Key words: instrumentation: polarimeters — methods: miscellaneous — Sun: chromosphere — techniques: polarimetric

1 Introduction

The polarization state of emitted light from the Sun contains a wealth of information on its magnetic fields. Polarimeters, which measures polarization information in spectral lines, play a crucial role in inferring solar magnetic fields via Zeeman and Hanle effects (Hale 1908; del Toro Iniesta 2003; Stenflo 2003, 2013; Hough 2005; Lin 2009). In recent years, studies in solar physics show that more and more attention is shifting from the Sun's photosphere towards the chromosphere, transition region, and corona (Casini et al. 2005; López Ariste et al. 2005; Lin 2005; Tomczyk et al. 2007; Cargill 2009; Yamamoto & Sakurai 2009; Ramelli et al. 2011; Trujillo Bueno et al. 2011; Judge et al. 2013; Orozco Suárez et al. 2014; Wiegelmann et al. 2014; Milić et al. 2017; Grechnev et al. 2019; Hu et al. 2019). Prominences (also known as filaments), suspended by complex magnetic fields, are large-scale structures of cool plasma embedded in the million-degree hot corona. Because the magnetic field is the most important force that drives their formation, structuring, and eruption (Paletou & Aulanier 2003), spectropolarimetry of prominences and filaments is not only important in deriving their magnetic fields, but also has great significance in studying the structure and evolution of the coronal magnetic field (Elmore et al. 2008; Rimmele et al. 2014).

Currently, the polarimeter is an indispensible scientific instrument for modern solar telescopes (Mártinez Pillet et al. 1999; Qu et al. 2001; Beck et al. 2005; Cao et al. 2006; Socas-Navarro et al. 2006; Zhang et al. 2007; Balthasar et al. 2011; Elmore 2011; Goode & Cao 2012; Deng, Liu & CGST Group 2012; Hanaoka 2012; Collados et al. 2013; Penn 2014; Schmidt et al. 2014; Liu et al. 2014; Iglesias et al. 2016; Anan et al. 2018; Sakurai et al. 2018), and currently there are some ground-based spectropolarimeters that can be used for measuring magnetic fields of prominences and filaments in the visible or near-infrared wavelengths; for instance, the Advanced Stokes Polarimeter (ASP, Skumanich et al. 1997) and the Diffraction-Limited Spectro-Polarimeter (DLSP, Sankarasubramanian et al. 2004) at the Dunn Solar Telescope, Multi-line spectropolarimetry mode at the Téléscope Heliographique pour l'étude du Magnetisme et des Instabilités Solaires (THEMIS/MTR, Paletou & Molodij 2001), etc. These polarimeters employ conventional mechanical modulation which uses a rotating retarder, such as quartz or a polymer wave plate, as the polarization modulator; due to the low modulation frequency, a dual beam configuration is normally adopted to overcome the seeing-induced crosstalk.

Meanwhile, some other spectropolarimeters choose liquid crystal retarders for fast polarization modulation (Jaeggli et al. 2010; Guo et al. 2017; Ren et al. 2020), especially the ferroelectric liquid crystal retarders (FLCs) which are very promising alternatives to the conventional rotating wave plates (Hanaoka 2004; Hough 2005; Xu et al. 2006; Hou et al. 2013; Feller et al. 2014). First, FLCs are bistable, electrically switchable wave plates, therefore, they have no moving parts and FLCs-based polarimeters do not suffer from the image wander that is commonly seen in rotating-retarder polarimeters (Peinado et al. 2013). Secondly, FLCs have an extremely fast response with a typical time of $\sim$100 μs, which allows a modulation frequency of up to 1 kHz that is much higher than the frequency range of seeing (Ramelli et al. 2014). As most of the seeing power contained in the 1–100 Hz frequency range (Judge et al. 2004), a modulation frequency of the order of 100 Hz can drastically suppress the spurious polarization caused by the seeing (Lites 1987; Nagaraju et al. 2011; Nagaraju & Feller 2012; Feller et al. 2014; Nagata et al. 2014), and a single beam configuration becomes possible which uses the same physical pixels for each differential polarization measurement, so it is free from differential effects which typically exist in the dual beam system, such as differences in the transmissions and aberrations of the two beams and the gain table calibration of the detector(s) (Ramelli et al. 2010; Snik et al. 2014). Thirdly, FLCs have long life spans; past experience has shown that FLCs of approximately 25 mm diameter have lifetimes of over 10 years (Streander et al. 2008). At present, there are a number of FLC-based spectropolarimeters for prominence and filament research, such as the Zürich Imaging Polarimeter (ZIMPOL, Gandorfer 1999; Gandorfer et al. 2004; Ramelli et al. 2010, 2014) at the Gregory-Coudé telescope of Istituto Ricerche Solari Locarno, the Tenerife Infrared Polarimeter (TIP, Collados et al. 2007) at the Vacuum Tower Telescope, the Synoptic Optical Long-term Investigation of the Sun/Vector Spectromagnetograph (SOLIS/VSM, Keller & Solis Team 2001; Keller et al. 2003; Streander et al. 2008; Henney et al. 2009; Gosain & Harvey 2014) at the Kitt Peak Vacuum Telescope (now relocated to the New Solar Telescope of the Big Bear Solar Observatory), etc. Among them, ZIMPOL with FLC modulators is able to operate a modulation frequency as high as 1 kHz, and a dedicated CCD sensor equipped with a microlens array and a mask is employed as the synchronous demodulator. In the TIP, the modulation frequency is 2 Hz. The SOLIS/VSM system does full polarimetry up to 75 times per second. Furthermore, the total polarimetric efficiencies of current FLC-based polarimeters are commonly above 80% (Iglesias et al. 2016).

In this work, a High speed and high efficiency Imaging POlarimeter (HIPO) is proposed based on a pair of FLCs, and the scientific goal of the HIPO is to carry out full Stokes spectropolarimetry of prominences and filaments in the visible wavelength from the ground. A unique

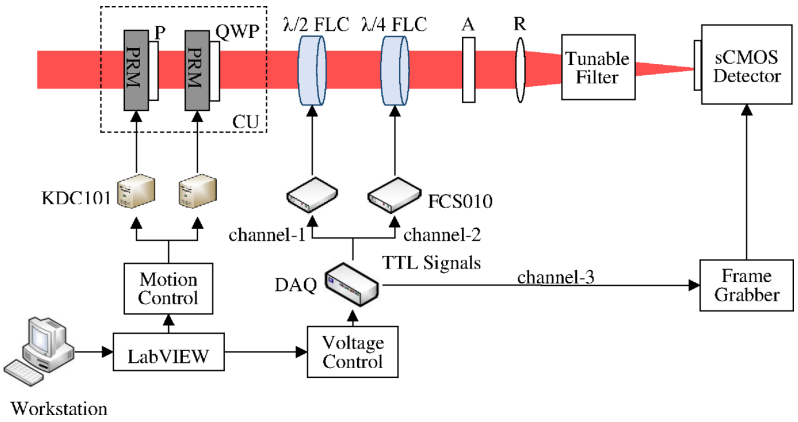

Fig. 1. Schematic diagram of the HIPO. P: polarizer, QWP: quarter-wave plate, PRM: motorized precision rotation mount, CU: calibration unit, FLC: ferroelectric liquid crystal, A: analyzer, R: re-imaging lens, DAQ: data acquisition device, KDC101: k-cube brushed DC servo motor controller, FCS010: liquid crystal controller. (Color online)

feature of the HIPO is that it enables high cadence polarization measurements covering a wide FOV; such observations are impossible for spectropolarimeters attached to large solar telescope, even though some of them have much higher spatial and spectral resolutions and sensitivities, and they observe various kinds of scientific targets. In the HIPO, the modulation frequency can achieve ∼100 Hz which greatly suppresses the seeing-induced crosstalk, and a single beam setup is used. In addition, the HIPO is able to deliver a maximum FOV of $62'' \times 525''$, which is sufficient for scientific targets of prominences and filaments as most of their sizes are typically within $8'$ (López Ariste et al. 2005; Elmore et al. 2008). At the current stage, the HIPO is integrated with an Hα tunable filter and optimized for Hα wavelength, and a high polarimetric efficiency of 0.9861 is achieved. Compared with most other representative ground-based solar polarimeters, the HIPO shows advantages in aspects of modulation frequency and polarimetric efficiency. We demonstrate that the HIPO system is capable of performing full Stokes polarimetry with an accuracy better than 2.7×10^{-3} in the observations. The remainder of this paper is arranged as follows. Section 2 provides a detailed description of system configuration and algorithms. Section 3 introduces experimental procedures. Section 4 presents the polarimetry results and associated discussion. Finally, the conclusions are given in section 5.

2 Instrument design

2.1 System overview

A schematic diagram of the HIPO is shown in figure 1. The modulation package consists of a λ/2 FLC and a λ/4 FLC (at Hα wavelength, 6562.8 Å) manufactured by Meadowlarks Optics, and each FLC is operated through a separate controller. The analyzer is a Glan–Thompson polarizer with high extinction ratio ($>10^5$:1 in the 430–700 nm) manufactured by Newport. A DayStar Hα tunable filter is integrated with the polarimeter, and a high-speed and low-noise Andor Zyla 5.5 scientific CMOS camera is used to record modulated images under the global shutter mode. In order to realize high-speed polarimetry, a multi-channel data acquisition device (DAQ) manufactured by National Instruments acts as an external trigger source to control and synchronize the FLCs and the sCMOS detector. Each image is automatically saved as a binary file that takes up at least half the size of other file formats, such as FITS or TXT; this not only saves space for data storage, but also consumes less time for data reduction. A calibration unit (CU) consisting of a linear polarizer and a quarter-wave plate is used to calibrate instrumental polarization, and the two polarization components of the CU are mounted on to an individual motorized precision rotation mount. During the polarimetry observations, the CU will be removed from the optical train. Furthermore, we developed dedicated LabVIEW software to control the HIPO system via a workstation.

2.2 Modulation scheme

In order to derive full Stokes parameters $(I, Q, U, V)^T$, at least four polarization images should be employed. As the FLC is a bi-state retarder, we design four modulation states from the two FLCs, i.e., four pairs of fast-axis (f-axis) orientations. The modulation cycle of the HIPO is shown in table 1.

According to system configuration and modulation strategy, the input and output Stokes vectors represented by $S_{\rm in}$ and $S_{\rm out}$, respectively, can be expressed by Mueller calculus:

$$S_{\rm out} = M \cdot S_{\rm in} = \mathbf{M}_{\rm A} \cdot \mathbf{M}_{\rm FLC2} \cdot \mathbf{M}_{\rm FLC1} \cdot S_{\rm in}, \quad (1)$$

Table 1. Modulation cycle of the HIPO.

	λ/2 FLC			λ/4 FLC		
Modulation cycle	DAQ output	Controller output	F-axis orientation	DAQ output	Controller output	F-axis orientation
1	0.0 V	−15.0 V	0°	0.0 V	−15.0 V	0°
2	5.0 V	15.0 V	∼45°	0.0 V	−15.0 V	0°
3	5.0 V	15.0 V	∼45°	5.0 V	15.0 V	∼45°
4	0.0 V	−15.0 V	0°	5.0 V	15.0 V	∼45°

$$\mathbf{M}_{\mathrm{FLC}}(\alpha,\delta) = \begin{Bmatrix} 1 & 0 & 0 & 0 \\ 0 & \cos^2 2\alpha + \sin^2 2\alpha\cos\delta & \cos 2\alpha\sin 2\alpha(1-\cos\delta) & -\sin 2\alpha\sin\delta \\ 0 & \cos 2\alpha\sin 2\alpha(1-\cos\delta) & \sin^2 2\alpha + \cos^2 2\alpha\cos\delta & \cos 2\alpha\sin\delta \\ 0 & \sin 2\alpha\sin\delta & -\cos 2\alpha\sin\delta & \cos\delta \end{Bmatrix}, \tag{2}$$

$$\mathbf{M}_{\mathrm{A}}(\beta) = \frac{1}{2}\begin{Bmatrix} 1 & \cos 2\beta & \sin 2\beta & 0 \\ \cos 2\beta & \cos^2 2\beta & \cos 2\beta\sin 2\beta & 0 \\ \sin 2\beta & \cos 2\beta\sin 2\beta & \sin^2 2\beta & 0 \\ 0 & 0 & 0 & 0 \end{Bmatrix}, \tag{3}$$

where M is the Mueller matrix of the HIPO, $\mathbf{M}_{\mathrm{FLC}}$ and $\mathbf{M}_{\mathrm{A}}$ are Mueller matrices of the FLC and the analyzer, respectively, α and δ are the f-axis orientation and retardance of the LFC, respectively, and β is the transmission-axis (t-axis) orientation of the analyzer. The azimuth angles of the λ/2 FLC, λ/4 FLC and analyzer are 27.°3, 62.°5, and 75.°2 respectively, which are determined by an optimization process aiming to achieve the maximum polarimetric efficiency (more details can be found in subsection 3.2).

The modulation matrix **O** can be obtained by using equations (1)–(3):

$$\mathbf{O} = \begin{Bmatrix} 1.0000 & 0.5542 & 0.0314 & -0.8318 \\ 1.0000 & -0.9776 & 0.0550 & -0.2032 \\ 1.0000 & 0.3045 & 0.7975 & 0.5208 \\ 1.0000 & 0.2662 & -0.7694 & 0.5807 \end{Bmatrix}, \tag{4}$$

The demodulation matrix **D** is then calculated as

$$\mathbf{D} = \begin{Bmatrix} 0.2475 & 0.2781 & 0.2182 & 0.2562 \\ 0.3861 & -0.7092 & 0.1758 & 0.1473 \\ -0.0343 & 0.0121 & 0.6494 & -0.6272 \\ -0.6487 & -0.1377 & 0.4040 & 0.3824 \end{Bmatrix}, \tag{5}$$

Finally, the four Stokes parameters I, Q, U, and V can be retrieved from the polarization images I_{1-4} using equation (5) as

$$\begin{cases} I = 0.2475L_1 + 0.2781L_2 + 0.2182L_3 + 0.2562L_4, \\ Q = 0.3861L_1 - 0.7092L_2 + 0.1758L_3 + 0.1473L_4, \\ U = -0.0343L_1 + 0.0121L_2 + 0.6494L_3 - 0.6272L_4, \\ V = -0.6487L_1 - 0.1377L_2 + 0.4040L_3 + 0.3824L_4. \end{cases} \tag{6}$$

3 Experimental procedures

3.1 FLC calibrations

Theoretically, retardances of the λ/2 FLC and λ/4 FLC should equal π and $\pi/2$, respectively, and their switching angles are 45°. However, the practical values will depart from the nominal ones due to error in the manufacturing and assembly process. As a consequence, the actual properties of the two FLCs need to be calibrated in our work. First, the switching angles of the two FLCs were obtained by a standard calibration procedure based on transmitted intensity, and a drive voltage was operated at 1 Hz to the FLC which is slow enough to determine the f-axis orientation. Thus, the switching angle can be calculated from the difference of the two f-axis orientations. Secondly, the FLC was placed between a pair of polarizers and its f-axis was rotated by 45° with respect to the t-axis of the first polarizer. In this manner, retardances under low and high states were calibrated individually, which can be computed by

$$\delta = \arccos(I_{c1} - I_{c2}/I_{c1} + I_{c2}), \tag{7}$$

where I_{c1} and I_{c2} are the transmitted intensities when the two polarizers are parallel and perpendicular, respectively. The calibration results for the two FLCs are summarized in table 2.

Table 2 reveals that the switching angles of the two FLCs are 45°12′ and 42°15′, respectively, and retardances under low and high states of each FLC show a difference of a few degrees; this is neglected in most works. Based on the above calibration results, we optimized the polarimetric efficiency and calibrated modulation matrix accordingly, shown as equation (4).

3.2 Polarimetric efficiency optimization

It is worth noting that polarimetric efficiency will decline due to the actual properties of the FLCs differing from their theoretical values, e.g., differences of switching angle and retardance which is unavoidable in the manufacturing of the FLCs (Hanaoka 2004). In this work, an optimization was performed based on the FLC calibration results and constrained nonlinear minimization approach, with the

Table 2. Calibration results of the two FLCs.

Component	Switching angle	Retardance @ low-state	Retardance @ high-state
λ/2 FLC	45°12′ ± 26′	215°20′ ± 23′	209°02′ ± 48′
λ/4 FLC	42°15′ ± 08′	96°09′ ± 16′	91°01′ ± 23′

goal of achieving the maximum polarimetric efficiency according to polarization components that the HIPO used. In the optimization, azimuth angles of the two FLCs and the analyzer are chosen as three variables to be optimized. As the total efficiency should be no greater than unity, we define an objective function (OF) for the optimization as

$$OF = 1 - \xi_{\text{total}} = 1 - \sqrt{\xi_Q^2 + \xi_U^2 + \xi_V^2}, \tag{8}$$

$$\xi_i = \left[n \sum_{j=1}^{N} D_{i,j}^2(\theta_1, \alpha_1, \delta_{1,\text{low}}, \delta_{1,\text{high}}, \theta_2, \alpha_2, \delta_{2,\text{low}}, \delta_{2,\text{high}}, \theta_3) \right]^{-1/2}, \tag{9}$$

where ξ_{total} and ξ_i are efficiencies of the system and the ith Stokes parameter, respectively, and ξ_i is constrained to $\xi_i \geq 0.5$ during the optimization, D is the demodulation matrix, θ_1, θ_2, and θ_3 are azimuth angles of the λ/2 FLC, λ/4 FLC, and the analyzer, respectively, and their lower and upper boundaries are limited to $[0, 2\pi]$, and (α, δ) are the switching angle and retardance respectively.

According to equation (8), the higher the polarimetric efficiency achieved, the smaller the value of the OF becomes. This implies that when the HIPO has the maximum efficiency, the value of the OF reaches the minima and should approach to zero. Therefore, the goal of the optimization is to determine values of θ_1, θ_2, and θ_3 which result the minimum value of the OF. The curve of the optimization process is shown in figure 2.

Figure 2 shows that the value of the OF is decreasing in the optimization procedure, and the final value turns to 0.002626 after 152 iteration steps. Optimum azimuth angles of the λ/2 FLC, λ/4 FLC, and analyzer are determined as $(\theta_1, \theta_2, \theta_3) = (27.^\circ3, 62.^\circ5, 75.^\circ2)$, and polarimetric efficiencies of the Stokes Q, U, and V are optimized as $(\xi_Q, \xi_U, \xi_V) = (0.5957, 0.5534, 0.5777)$, which reveals that all the efficiencies are beyond 0.5 and a good balance of efficiency between each Stokes parameter is realized. The optimized total efficiency is $\xi_{\text{total}} = 0.9974$, very close to the maximum efficiency of 1.0.

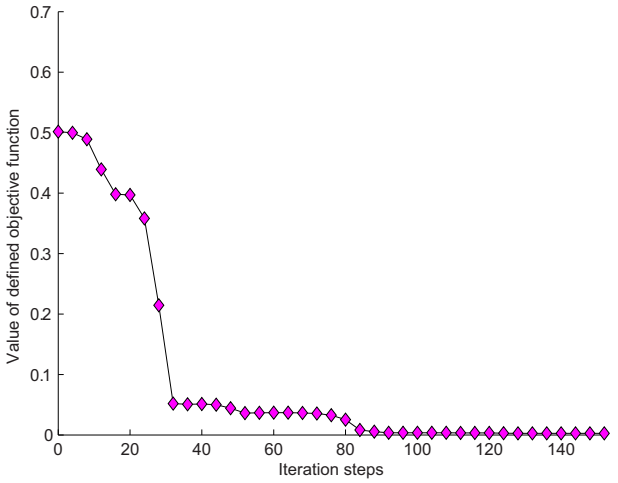

Fig. 2. Values of objective function $1 - \xi_{\text{total}}$ in the polarimetric efficiency optimization. (Color online)

3.3 System synchronization

When developing a high-speed FLC-based polarimeter, it is crucial to synchronize working states between the FLCs and the detector, because any image recorded under an incorrect modulation state will undoubtedly harm the measurement accuracy of the Stokes parameters. In the HIPO system, a multi-channel DAQ is introduced to control and synchronize the FLCs and the sCMOS detector; specifically, three digital output channels (channel-1, channel-2, and channel-3) are generated in the DAQ, and signals in channel-1 and channel-2 are used to drive the two FLC controllers separately, while the signal in channel-3 is employed to trigger the sCMOS detector, as shown in figure 3.

Frequencies of transistor transistor logic (TTL) signals in the three channels are designed as $f_{\text{channel-1}}:f_{\text{channel-2}}:f_{\text{channel-3}} = 1:1:4$. Channel-1 is the reference signal, and channel-2 and channel-3 are triggered by channel-1 with the manner shown in figure 4. After triggering from channel-1, channel-2 and channel-3 generate the pulses independently, both with a phase delay of $\pi/2$ from channel-1 until next trigger. Thus, channel-3 will trigger the detector once at every falling edge of the reference signal in channel-1, and the detector can sequentially grab four images under four desired modulation states within every modulation cycle. A merit of this synchronization method is that it fulfills the maximum frame rate of the sCMOS detector; in addition, no time error is accumulated because the detector is precisely triggered once within each cycle. The frame rate of our Andor Zyla 5.5 sCMOS detector is able to achieve 400 frames s^{-1} when using a pixel area of 256 × 256; when keeping the detector at a high duty cycle of 95.0% and taking into account time for FLC response, we reasonably

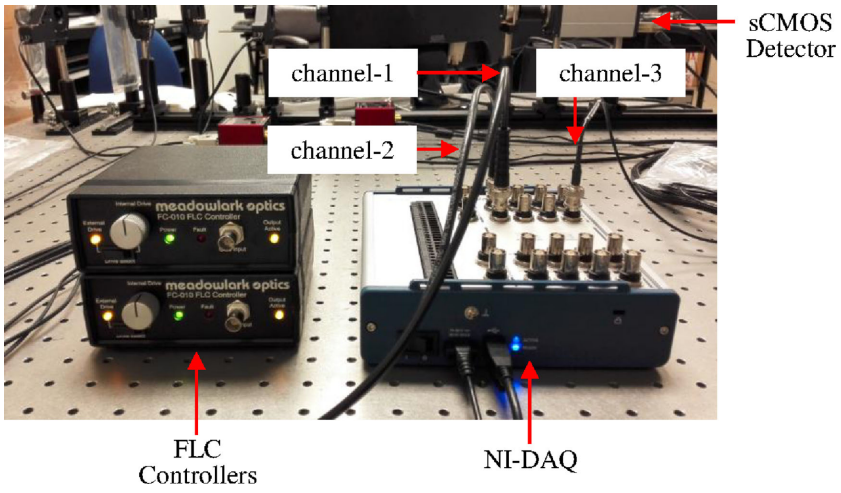

Fig. 3. System synchronization by using a multi-channel DAQ which generates signals in three channels to synchronize the two FLCs and the sCMOS detector. (Color online)

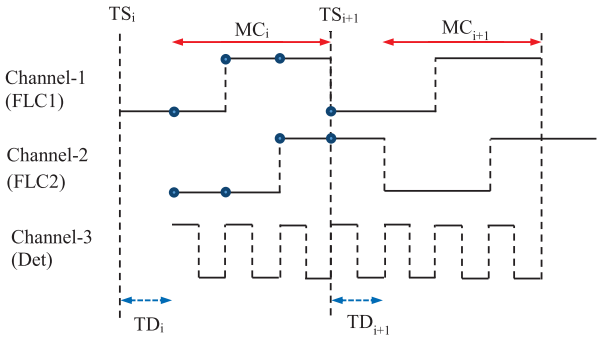

Fig. 4. Schematic diagram of designed TTL signals in three channels to realize proposed modulation scheme and system synchronization. TS: trigger start, TD: time delay, MC: modulation cycle; i is the sequence number. (Color online)

reduce the frame rate to 380 frames s^{-1}, so a modulation frequency of 95 Hz is achieved.

We have fully validated the performance of the synchronization method, and the results are shown in figure 5. For one FLC test, we change the phase delay of the FLC channel from $\pi/2$ to zero, because two images under each FLC state can be grabbed starting from the first trigger in this fashion. For the two-FLC test, however, the phase delays of the FLC channels are kept as $\pi/2$, which is the same situation as the actual polarimetry measurements by the HIPO. Please note that changing the value of the phase delay will not affect the verification of the system synchronization.

Figure 5a shows that when testing with one FLC ($\lambda/2$ FLC for example), the detector was successfully triggered twice and two images were recorded under each FLC state; this is in accordance with the frequency ratio between different channels. Additionally, synchronization was confirmed by operating the FLC at frequencies ranging from 25 to 95 Hz. A higher modulation frequency means exposure time becomes shorter, which leads to lower image intensities. Figure 5b reveals that when testing the two FLC together ($\lambda/2$ FLC and the $\lambda/4$ FLC), the detector took four desired images within every modulation cycle, and intensities of recorded images demonstrates that no disorder or mismatch occurs during the modulation. System synchronization is stably operated at a high modulation frequency of 95 Hz. In our test, measured intensities under the same modulation state were found to have a little fluctuation; this is because the halogen lamp light source (model: Thorlabs OSL1) we used in the laboratory is not a stabilized one.

3.4 System integration and instrumental polarization calibration

For the system integration, we made two dedicated aluminum cylinder interfaces. One is for housing the two FLCs and the polarizer and then it connects to the telescope's telecentric amplifier (focal extender) and the tunable filter, while the other one is for connecting the tunable filter and the sCMOS detector. Configuration of the HIPO is very compact, as shown in figure 6.

The CU is then placed in front of the HIPO and a group of known input Stokes vectors are generated. The polarizer is oriented at 0°, and the quarter wave plate is rotated from 0° to 180° in 5° steps. In this way, the response matrix of the system can be determined by comparing the known inputs and measured outputs of the Stokes vectors. In order to achieve a high calibration accuracy, the retardance of the quarter wave plate is calibrated beforehand, which is 82°10′ ± 46′ at 656.3 nm. Calibration curves of each Stokes parameter are shown in figure 7. The discrepancy between the measured and calculated polarization signals is due to intensity fluctuation of the light source, as well as possible misalignment of the components in the CU.

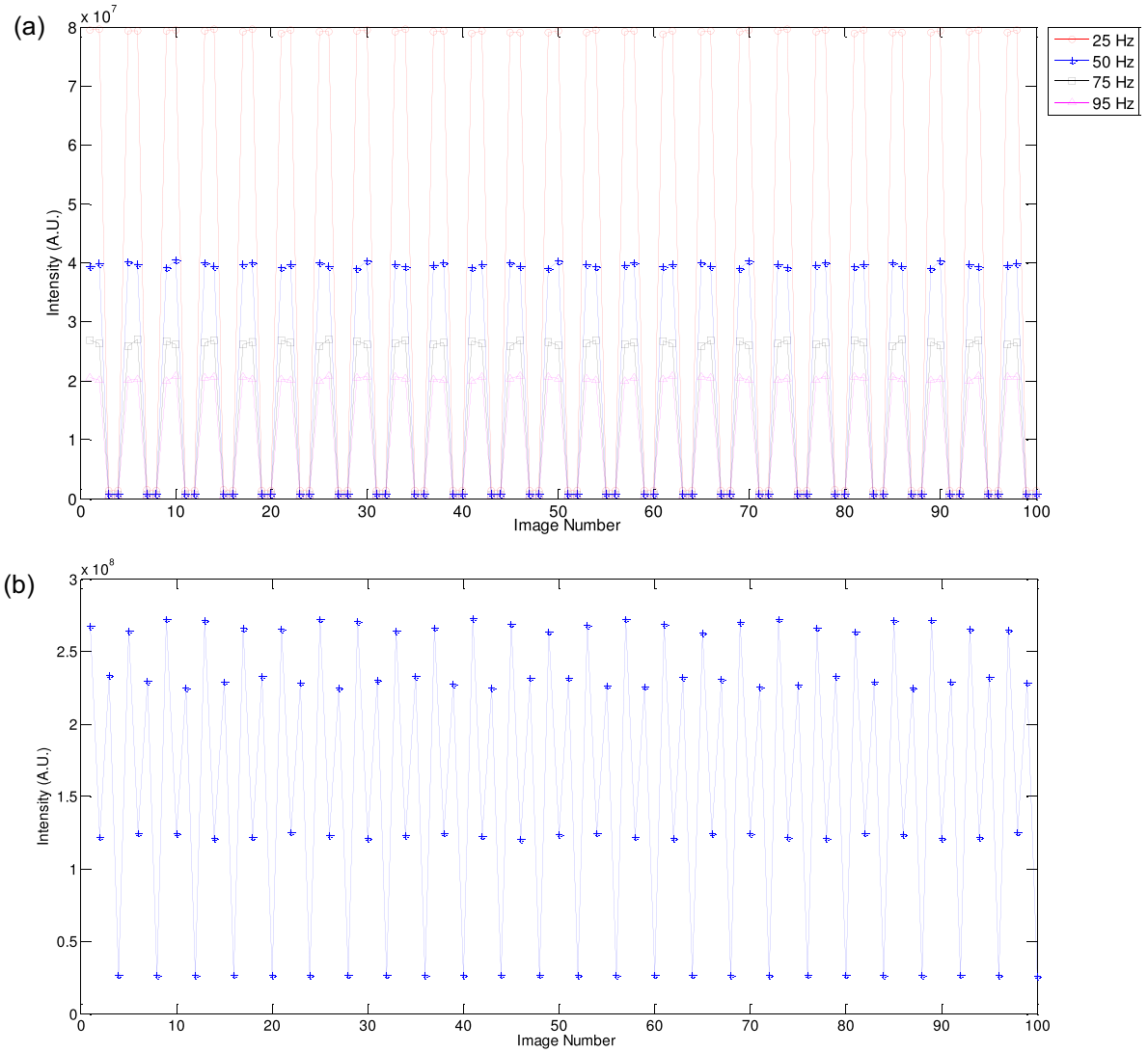

Fig. 5. System synchronization validations by checking recorded intensities; "A.U." on the *y*-axis stands for Arbitrary Unit. (a) One FLC, operated at different frequencies ranging from 25–95 Hz; (b) Two FLCs, operated at 95 Hz under proposed modulation. (Color online)

The response matrix of the HIPO system is derived as

$$\mathbf{X} = \begin{Bmatrix} 1.0000 & 0.0000 & 0.0000 & 0.0000 \\ -0.0044 & 0.9966 & 0.0149 & 0.0076 \\ 0.0011 & 0.0074 & 0.9730 & 0.0051 \\ -0.0029 & 0.0046 & -0.0022 & 0.9952 \end{Bmatrix}. \quad (10)$$

When using response matrix **X** and the modulation matrix presented in subsection 2.2, practical efficiencies of the Stokes Q, U, and V are obtained as $(\xi_{Q'}, \xi_{U'}, \xi_{V'}) = (0.5934, 0.5385, 0.5747)$, which are slightly below the optimized values but still very high; the total efficiency is $\xi_{\text{total}'} = 0.9861$.

Finally, the HIPO system is installed on a 8-inch-aperture Hα solar telescope, as shown in figure 8. The advantage of this configuration is that it is almost free of the telescope polarization because its Cassegrain focus is used and the geometric symmetry is preserved well. The Hα solar telescope is modified based on a Celestron's EdgeHD C8 optical tube assembly by AiryLab, and a specific di-eletric coating was applied on to the corrector plate which acts as energy rejection filter and passes only 120 nm FWHM bandwidth inside the telescope, thus dramatically limiting the heat. The secondary mirror stays cool and its support is protected from direct exposition to the Sun's light by a white plastic cap. The optical density is above 3 below 530 nm and above 780 nm up to 1100 nm in the short wave infrared, which protects the FLCs from damage by the solar ultraviolet radiation. The effective transmission in the Hα band is about 85%. In addition, a

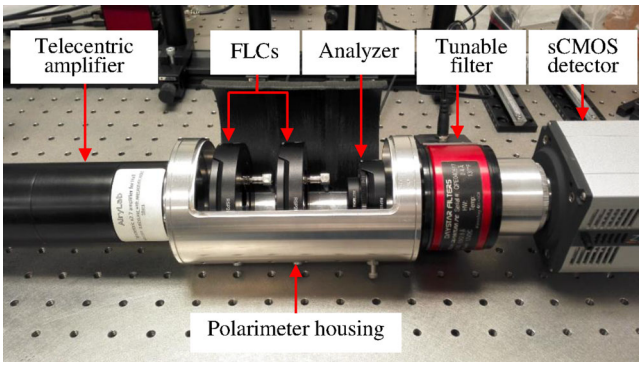

Fig. 6. Key components of the HIPO and system integration. (Color online)

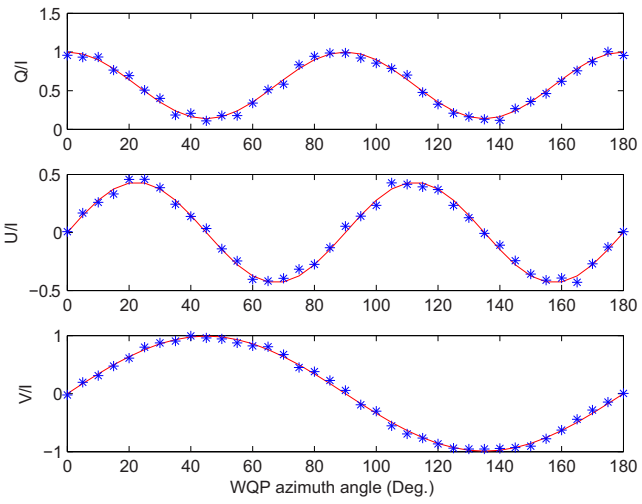

Fig. 7. Instrumental polarization calibration results. Solid line: generated calibration vector; dotted line: measured Stokes vector. (Color online)

specifically optimized telecentric amplifier (focal extender) $\times$ 2.759 brings the incoming rays to a geometry compatible with the unobstructed Fabry Perrot Hα etalon, resulting in the F-number of the Hα solar telescope of 27.59.

4 Results and discussion

Several rounds of full Stokes Hα imaging polarimetry of the chromosphere were conducted, and the telescope was randomly pointed to the disk area of the quiet Sun. The modulation frequency of the HIPO is 95 Hz and the exposure time of each image is 2.37 ms; 500 images are grabbed under each modulation state, so a total of 2000 images are recorded in the full modulation cycle. According to the system configuration and a pixel area of 256 $\times$ 256 with a pixel size of 6.5 μm $\times$ 6.5 μm, an FOV of 62″ $\times$ 62″ is delivered. However, one should note that the detector has a full array size of 2560 $\times$ 2160, and its frame rate is able to reach 400 fps when selecting a pixel area of 256 $\times$ X (changing dimension X will not affect the frame rate). In other words, a maximum pixel area of 256 $\times$ 2160, corresponding to a FOV of 62″ $\times$ 525″, can be selected for polarimetry measurements without sacrificing the maximum frame rate; therefore, the modulation frequency of 95 Hz can be maintained. Dark subtraction and flat-fielding are included in the data reduction, and polarimetry results of the chromosphere are shown in figure 9.

Figure 9 reveals that features of the chromosphere can be clearly observed in Stokes I images, and results of each Stokes parameter are averaged over 500 Stokes images. In regions of the quiet Sun, panels (a)–(c) show Hα polarimetry images of Q/I, U/I and V/I that are very uniform, and root-mean-square (rms) noise levels of them are better than 1.1 $\times$ 10^{-3}, 2.7 $\times$ 10^{-3}, and 1.9 $\times$ 10^{-3}, respectively. The results indicate that the HIPO is able to deliver a good measurement accuracy with a single beam configuration, thanks to the high modulation frequency and polarimetric efficiency. Furthermore, polarimetry results of the solar limb is used to demonstrate the seeing-induced crosstalk, because the seeing-induced spurious polarization signals appear where the brightness gradient is steep. In this work, we randomly picked two regions for the analysis, which are denoted by the small white rectangles shown in panel (d), and the method to evaluate effects caused by the seeing is introduced in Nagaraju and Feller's research (Nagaraju & Feller 2012), i.e., computing the value of the crosstalk term from Stokes parameter i to r by using the equation $C_{ri} = \langle|r|\rangle/\langle|i|\rangle$, where r is Stokes Q, U, or V, and i is Stokes I, $|...|$ means absolute value, and $\langle...\rangle$ implies the average over the rectangular boxes marked on images. Our results show that the seeing-induced crosstalk is approximately 1.0 $\times$ 10^{-3}, which is consistent with the results presented in Nagaraju and Feller's publication, as they estimate the seeing-induced crosstalk for the polarimeter in a single-beam setup is of the order of 10^{-3} when using a modulation frequency of $\sim$100 Hz. In addition, they pointed out that if the modulation frequency could be increased to $\sim$200 Hz, the crosstalk values should be of the order of 10^{-4} or less. In our HIPO system, double the modulation frequency can be achieved by using half the current FOV, and the test will be carried out in a future phase of the system upgrade and optimization.

In what follows, we conduct discussions on the aspects of polarimetric efficiency comparison, imaging quality improvement, and system flexibility. First, polarimetric efficiencies of the HIPO and other representative ground-based solar polarimeters are listed in table 3.

Table 3 shows that the HIPO has the capability to offer a well-balanced efficiency and deliver a total efficiency as high as 0.9861, which displays an obvious advantage over the efficiencies of most other representative ground-based

Fig. 8. HIPO system mounted to a 200-mm Hα solar telescope for polarimetry observation. (Color online)

solar polarimeters. Although SOLIS/VSM and SPs also have high total efficiencies, the former achieves full polarimetry to 75 Hz while the HIPO is about 27% faster, and the latter is only designed to measure linearly polarized Stokes Q and U in observation mode, while the HIPO measures both linearly and circularly polarized Stokes Q, U, and V in the observations.

Secondly, the AiryLab 8-inch Hα telescope is optimized for a back focus ranging from 100 to 250 mm without impact on the optical performances. At present, the total length of the polarimeter system is approximately 270 mm, which leads to a small degradation of the imaging quality. In the next phase, two new aluminum cylinder interfaces will be made, which are shortened by removing redundant spaces; lengths of 30 mm and 18 mm, respectively, are estimated to be cut. As a consequence, the total length of the updated HIPO system will become approximately 222 mm, and the imaging quality is expected to be greatly improved.

Thirdly, the current HIPO system is optimized and tested for observing at Hα wavelengths, but the system configuration, optimization method, and hardware control approach proposed in this paper are highly transferable; e.g. if other spectral lines are required in future research, the HIPO can be replaced with optical components for the desired wavelengths. Furthermore, temperature control is not currently included because the polarimeter is a prototype and its development is implemented in our temperature-stabilized laboratory. In this work, we mainly focus on validating some conceptual tests of the HIPO, e.g., high-frequency modulation, synchronization, and polarimetry measurements, but temperature control will be added in the next phase of system upgrade, and the FLCs will be placed in a heat insulation housing and the temperature will be kept at 42°C (or a few centigrade higher), with a temperature stability of ± 0.1°C.

5 Conclusions

In this paper, a High speed and high efficiency Imaging POlarimeter (HIPO) is proposed based on FLCs, and a unique feature of the HIPO is that it has the capability to perform high-cadence polarization measurements covering a wide FOV. FLC retardances under low and high states were carefully calibrated, and they were found to have a slight discrepancy which is neglected in most works. In order to obtain the maximum polarimetric efficiency, calibrated results of the two FLCs and an optimization were performed based on a constrained nonlinear minimization approach. More specifically, optimized efficiencies of the Q, U, and V are well balanced and determined as $(\xi_Q, \xi_U, \xi_V) = (0.5957, 0.5534, 0.5777)$, yielding a total efficiency of 0.9974, while their practical efficiencies are measured as $(\xi_{Q'}, \xi_{U'}, \xi_{V'}) = (0.5934, 0.5385, 0.5747)$ which are very close to their optimized values, and a total

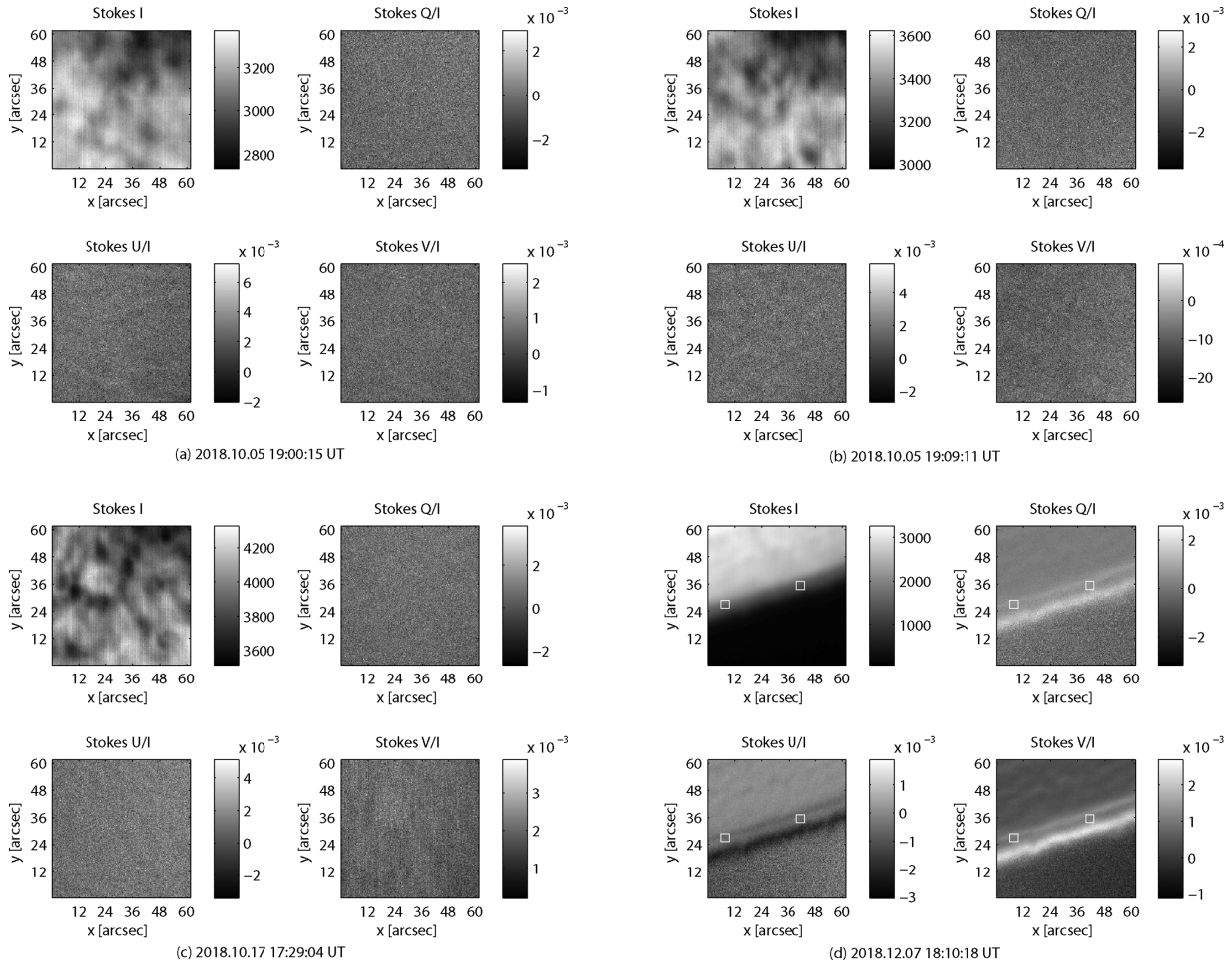

Fig. 9. Full Stokes *Hα* polarimetry: from panels (a) to (c) are the results of the solar disk and panel (d) is result of the solar limb. White rectangular boxes are the regions for seeing induced cross-talk analysis.

Table 3. Polarimetric efficiency comparison of different representative ground-based solar polarimeters.

Instruments	(ξ_Q, ξ_U, ξ_V)	ξ_{total}
ASP (Elmore et al. 1992)	(0.4100, 0.4100, 0.6100)	0.8416
LPSP & TIP (Mártinez Pillet et al. 1999)	(0.4500, 0.4500, 0.6700) & (0.6500, 0.5000, 0.4700)	0.9241 & 0.9452
SOLIS/VSM (Keller et al. 2003)	(0.57, 0.57, 0.57)	1.0000
DLSP (Sankarasubramanian et al. 2004)	(0.4887, 0.4864, 0.4840)	0.8424
FLC polarimeter (Hanaoka 2004)	(0.2574, 0.2184, 0.4710)	0.5795
POLIS (Beck et al. 2005)	(0.4940, 0.4640, 0.4960)	0.8398
SPINOR (Socas-Navarro et al. 2006)	(0.5383, 0.4885, 0.4829)	0.8727
PA (Xu et al. 2006)	(0.7187, 0.4610, 0.4584)	0.9691
ZIMPOL (Ramelli et al. 2010)	(0.5000, 0.3500, 0.3500)	0.7100
VIP (Beck et al. 2010)	(0.5300, 0.5200, 0.5600)	0.9300
SPs (Hou et al. 2013)	(0.7000, 0.7200, —) & (0.6700, 0.7100, —)	1.000 & 0.9762
FSP (Feller et al. 2014)	(0.5300, 0.4900, 0.5000)	0.8781
HIPO (this paper)	(0.5934, 0.5385, 0.5747)	0.9861

efficiency of 0.9861 is achieved. It is concluded that the HIPO shows evident advantages in terms of modulation frequency and polarimetric efficiency compared with most other representative ground-based solar polarimeters. In the present configuration, it is demonstrated that we achieved a polarimetric accuracy better than 2.7×10^{-3} in the visible channel at Hα wavelengths, and this allows us to assess the actual performance of the new measurement concept in a single beam configuration, as well as to gain practical experience that will be valuable for the future project phase.

Our work lays a foundation for developing high-speed and high-accuracy polarimeters for our next-generation solar instruments.

Acknowledgments

We are grateful to the referee for insightful and valuable comments which improves the manuscript. J. Guo acknowledges the supports from the National Natural Science Foundation of China (NSFC) under Grant Nos. 11703058 and U2031210, the Strategic Priority Research Program of Chinese Academy of Sciences, Grant No. XDA15011100, and the Strategic Pioneer Program on Space Science, Chinese Academy of Sciences, Grant No. XDA15011100. Y. T. Zhu acknowledges the support from the NSFC under Grant No. 11827804. X. Zhang acknowledges the NSFC support under Grant No. 11673042.

Conflict of interest

The authors declare that there are no conflicts of interest.

References

Anan, T., et al. 2018, PASJ, 70, 102
Balthasar, H., et al. 2011, ASP Conf. Ser., 437, 351
Beck, C., Bellot Rubio, L. R., Kentischer, T. J., Tritschler, A., & Del Toro Iniesta, J. C. 2010, A&A, 520, A115
Beck, C., Schmidt, W., Kentischer, T., & Elmore, D. 2005, A&A, 437, 1159
Cao, W., Jing, J., Ma, J., Xu, Y., Wang, H., & Goode, P. R. 2006, PASP, 118, 838
Cargill, P. J. 2009, Space Sci. Rev., 144, 413
Casini, R., Bevilacqua, R., & López Ariste, A. 2005, ApJ, 622, 1265
Collados, M., et al. 2013, in Highlights of Spanish Astrophysics VII, ed. J. C. Guirado et al. (Barcelona: Spanish Astronomical Society), 808
Collados, M., Lagg, A., Díaz Garcí A, J. J., Hernández Suárez, E., López López, R., Páez Mañá, E., & Solanki, S. K. 2007, ASP Conf. Ser., 368, 611
del Toro Iniesta, J. C. 2003, Introduction to Spectropolarimetry (Cambridge: Cambridge University Press), ch. 5
Deng, Y., Liu, Z., & CGST Group, 2012, ASP Conf. Ser., 463, 405
Elmore, D. F. 2011, ASP Conf. Ser., 437, 309
Elmore, D. F., et al. 1992, SPIE Proc., 1746, 22
Elmore, D. F., Casini, R., Card, G. L., Davis, M., Lecinski, A., Lull, R., Nelson, P. G., & Tomczyk, S. 2008, SPIE Proc., 7014, 701416
Feller, A., Iglesias, F. A., Nagaraju, K., Solanki, S. K., & Ihle, S. 2014, ASP Conf. Ser., 489, 271
Gandorfer, A. M. 1999, Opt. Eng., 38, 1402
Gandorfer, A. M., Steiner, H. P. P. P., Aebersold, F., Egger, U., Feller, A., Gisler, D., Hagenbuch, S., & Stenflo, J. O. 2004, A&A, 422, 703
Goode, P. R., & Cao, W. 2012, SPIE Proc., 8444, 844403
Gosain, S., & Harvey, J. W. 2015, in IAU Symp. 305, Polarimetry: From the Sun to Stars and Stellar Environments, ed. K. N. Nagendra et al. (Cambridge: Cambridge University Press), 186
Grechnev, V. V., Kochanov, A. A., Uralov, A. M., Slemzin, V. A., Rodkin, D. G., Goryaev, F. F., Kiselev, V. I., & Myshyakov, I. I. 2019, Sol. Phys., 294, 139
Guo, J., Ren, D.-Q., Liu, C.-C., Zhu, Y.-T., Dou, J.-P., Zhang, X., & Beck, C. 2017, Res. Astron. Astrophys., 17, 8
Hale, G. E. 1908, ApJ, 28, 315
Hanaoka, Y. 2004, Sol. Phys., 222, 265
Hanaoka, Y. 2012, SPIE Proc., 8446, 844670
Henney, C. J., Keller, C. U., Harvey, J. W., Georgoulis, M. K., Hadder, N. L., Norton, A. A., Raouafi, N.-E., & Toussaint, R. M. 2009, ASP Conf. Ser., 405, 47
Hou, J., de Wijn, A. G., & Tomczyk, S. 2013, ApJ, 774, 85
Hough, J. H. 2005, ASP Conf. Ser., 343, 3
Hu, H., Liu, Y. D., Zhu, B., Peter, H., He, W., Wang, R., & Yang, Z. 2019, ApJ, 878, 106
Iglesias, F. A., Feller, A., Nagaraju, K., & Solanki, S. K. 2016, A&A, 590, A89
Jaeggli, S. A., Lin, H., Mickey, D. L., Kuhn, J. R., Hegwer, S. L., Rimmele, T. R., & Penn, M. J. 2010, Mem. Soc. Astron. Ital., 81, 763
Judge, P. G., Elmore, D. F., Lites, B. W., Keller, C. U., & Rimmele, T. 2004, Appl. Opt., 43, 3817
Judge, P. G., Habbal, S., & Landi, E. 2013, Sol. Phys., 288, 467
Keller, C. U., & Solis Team, 2001, ASP Conf. Ser., 236, 16
Keller, C. U., Harvey, J. W., & Solis Team, 2003, ASP Conf. Ser., 307, 13
Lin, H. 2005, ASP Conf. Ser., 343, 357
Lin, H. 2009, ASP Conf. Ser., 405, 413
Lites, B. W. 1987, Appl. Opt., 26, 3838
Liu, Z., et al. 2014, Res. Astron. Astrophys., 14, 705
López Ariste, A., et al. 2005, ApJ, 621, L145
Mártinez Pillet, V., et al. 1999, ASP Conf. Ser., 183, 264
Milić, I., Faurobert, M., & Atanacković, O. 2017, A&A, 597, A31
Nagaraju, K., & Feller, A. 2012, Appl. Opt., 51, 7953
Nagaraju, K., Feller, A., Ihle, S., & Soltau, H. 2011, SPIE Proc., 8148, 81480S
Nagata, S., et al. 2014, PASJ, 66, 45
Orozco Suárez, D., Asensio Ramos, A., & Trujillo Bueno, J. 2014, A&A, 566, A46
Paletou, F., & Aulanier, G. 2003, ASP Conf. Ser., 307, 458
Paletou, F., & Molodij, G. 2001, ASP Conf. Ser., 248, 617
Peinado, A., Lizana, A., & Campos, J. 2013, SPIE Proc., 8873, 88730S
Penn, M. J. 2014, Living Rev. Sol. Phys., 11, 2
Qu, Z. Q., Zhang, X. Y., Chen, X. K., Feng, Y. M., Gu, X. M., & Zhong, S. H. 2001, Sol. Phys., 201, 241
Ramelli, R., et al. 2010, SPIE Proc., 7735, 77351Y
Ramelli, R., Gisler, D., Bianda, M., Bello González, N., Berdyugina, S., & Soltau, D. 2014, SPIE Proc., 9147, 91473G
Ramelli, R., Trujillo Bueno, J., Bianda, M., & Asensio Ramos, A. 2011, ASP Conf. Ser., 437, 109
Ren, D., Han, Z., & Guo, J. 2020, Sol. Phys., 295, 109
Rimmele, T., Berger, T., Casini, R., Elmore, D., Kuhn, J., Lin, H., Schmidt, W., & Wöger, F. 2014, in IAU Symp. 300, Nature of Prominences and their role in Space Weather, ed. B. Schmieder et al. (Cambridge: Cambridge University Press), 362
Sakurai, T., et al. 2018, PASJ, 70, 58
Sankarasubramanian, K., et al. 2004, SPIE Proc., 5171, 207

Schmidt, W., Bell, A., Halbgewachs, C., Heidecke, F., Kentischer, T. J., von der Lühe, O., Scheiffelen, T., & Sigwarth, M. 2014, SPIE Proc., 9147, 91470E
Skumanich, A., Lites, B. W., Martínez Pillet, V., & Seagraves, P. 1997, ApJS, 110, 357
Snik, F., et al. 2014, SPIE Proc., 9099, 90990B
Socas-Navarro, H., Elmore, D., Pietarila, A., Darnell, A., Lites, B. W., Tomczyk, S., & Hegwer, S. 2006, Sol. Phys., 235, 55
Stenflo, J. O. 2003, SPIE Proc., 4843, 76
Stenflo, J. O. 2013, A&AR, 21, 66
Streander, K. V., Giampapa, M. S., Harvey, J. W., Henney, C. J., & Norton, A. A. 2008, SPIE Proc., 7014, 70147P
Tomczyk, S., McIntosh, S. W., Keil, S. L., Judge, P. G., Schad, T., Seeley, D. H., & Edmondson, J. 2007, Science, 317, 1192
Trujillo Bueno, J., Štěpán, J., & Casini, R. 2011, ApJ, 738, L11
Wiegelmann, T., Thalmann, J. K., & Solanki, S. K. 2014, A&AR, 22, 78
Xu, C. L., Qu, Z. Q., Zhang, X. Y., Jin, C. L., & Yan, X. L. 2006, Appl. Opt., 45, 8428
Yamamoto, T. T., & Sakurai, T. 2009, PASJ, 61, 75
Zhang, H.-Q., et al. 2007, Chin. J. Astron. Astrophys., 7, 281